A Weighted-Efficiency-Oriented Design Methodology of Flyback Inverter for AC Photovoltaic Modules

Anastasios C. Nanakos, Emmanuel C. Tatakis, *Member, IEEE*, and Nick P. Papanikolaou, *Senior Member, IEEE*

Abstract—An innovative design methodology that optimizes the weighted efficiency of a single-phase, single-stage flyback inverter for ac–photovoltaic (PV) module applications is proposed. This novel approach combines the essential advantages of the flyback topology with high-efficiency design in the direction of a reliable, cost-effective, and high-performance PV system. The proposed methodology focuses exclusively on choosing the inverter design parameters, taking into consideration the PV module characteristics and the topology operation constraints. In order to meet this goal, an analytical losses calculation should be performed. Since the problem is complicated, special effort is given to manipulate the equations and variables in such a way to minimize the number of parameters. The proposed methodology is also verified experimentally.

Index Terms—AC–photovoltaic (PV) module, dc–ac power conversion, design methodology, energy efficiency, losses, magnetic losses, MIC, microinverter, photovoltaic (PV) power systems.

Nomenclature

α, β, k	Parameters of the Steinmetz equation loss formula.
η_{CEC}	The weighted California Energy Commission (CEC) maximum power point tracking (MPPT) efficiency.
η_{EUR}	The weighted European MPPT efficiency.
η_w	Efficiency at the power level defined by w.
d_p	Peak duty cycle value of the primary semiconductor switch referring to the switching cycle that occurs at the time area of $\omega t = \pi/2$.
$d_{p,\max}$	Maximum d_p that occurs at the nominal power level.
f_s	Switching frequency of the primary switch (Hz).
i_{pri}	Instant current value of the primary transformer side (A).
i_{sec}	Instant current value of the secondary transformer side (A).

A. C. Nanakos and E. C. Tatakis are with the Department of Electrical and Computer Engineering, Laboratory of Electromechanical Energy Conversion, University of Patras, Rion-Patras 26504, Greece (e-mail: tnanakos@ece.upatras.gr; e.c.tatakis@ece.upatras.gr).

N. P. Papanikolaou is with the Department of Electrical Engineering, Technological Educational Institute of Lamia, Lamia 35100, Greece (e-mail: npapanikolaou@teilam.gr).

l_e	Effective length of the core (mm).
l_g	Length of the core air gap (mm).
n	Transformer turns ratio value.
r	Radius of the winding copper strand (mm).
$r_{\text{loss},w}$	Power loss ratio.
str_{pri}	Strands of the primary winding.
str_{sec}	Strands of the secondary winding.
$t_{f,\text{pri}}$	Current fall time of the switch on the primary transformer side (ns).
$t_{f,\text{sec}}$	Current fall time of the switch on the secondary transformer side (ns).
t_{OFF}	Primary switch OFF-time (s).
t_{ON}	Primary switch ON-time (s).
$t_{\text{ON},i}$	Primary switch ON-time for each switching cycle i (s).
$t_{\text{ON},p}$	t_{ON} interval value referring to the switching cycle that occurs at the time area of $\omega t = \pi/2$.
$t_{r,\text{pri}}$	Current rise time of the switch on the primary transformer side (ns).
$t_{r,\text{sec}}$	Current rise time of the switch on the secondary transformer side (ns).
$w(\%)$	Predefined power ratio according to European and CEC efficiency evaluation procedures.
A_e	Effective cross sectional area of the core (mm^2).
A_w	Window area of the core (mm^2).
$A_{w,\text{Cu}}$	Area of the winding window filled by copper (mm^2).
B_p	Maximum operational flux density (T).
B_{sat}	Saturation limit of the flux density (T).
C_f	Capacitance of the output filter (F).
C_{ff}	Percentage of the copper area over the entire winding window.
$C_{ff\max}$	Maximum allowed percentage of the copper area over the entire winding window.
DT	Temperature transformer rise (°C).
$DT_{\max}$	Maximum allowed transformer temperature rise (°C).
Fr_z	Resistance factor of the winding z.
$I_{\text{pri,avg}}$	Average current value of the primary transformer side (A).
$I_{\text{pri},p,i}$	Peak current value of the primary transformer side for each switching cycle i (A).
$I_{\text{pri,rms}}$	RMS current value of the primary transformer side (A).
$I_{\text{sec,avg}}$	Average current value of the secondary transformer side (A).

$I_{\mathrm{sec,rms}}$	RMS current value of the secondary transformer side (A).
$I_{\mathrm{sp},i}$	Peak current value of the main MOSFET for each switching cycle i (A).
$I_{z,\mathrm{avg}}$	Average current of the winding z.
$I_{z,\mathrm{rms}}$	RMS current of the winding z.
J	Current density of the tranformer windings (A/mm^2).
L_σ	Transformer leakage inductance (μH).
L_f	Inductance of the output filter (H).
L_1	Transformer primary inductance (μH).
N_{pri}	Number of turns of the transformer primary winding [photovoltaic (PV) side].
$P_{\mathrm{CL,pri}}$	Conduction losses of the semiconductor on the primary transformer side (W).
$P_{\mathrm{CL,sec}}$	Conduction losses of the semiconductor on the secondary transformer side (W).
P_{CPL}	Transformer copper losses (W).
P_{CRL}	Transformer core losses (W).
P_d	Conduction losses of the diode (W).
$P_{\mathrm{loss},w}$	Absolute value of power losses at the power level defined by w (W).
$P_{L\sigma L}$	Losses due to leakage inductance (W).
$P_{\mathrm{PV,nom}}$	Nominal inverter input power (W).
$P_{\mathrm{PV},w}$	Input power defined by ratio w (W).
$P_{\mathrm{SL,pri}}$	Switching losses of the semiconductor on the primary transformer side (W).
$R_{\mathrm{ac},z}$	Effective resistance of winding z.
R_d	Diode resistance (Ω).
$R_{\mathrm{dc},z}$	Resistance at direct current of constant value.
$R_{\mathrm{ds,ON}}$	ON-resistance of the transistor (Ω).
$R_{\mathrm{ds,pri}}$	ON-resistance of the transistor on the primary transformer side (Ω).
$R_{\mathrm{ds,sec}}$	ON-resistance of the transistor on the secondary transformer side (Ω).
R_t	Thermal resistance from the external ambient to the central hot spot (°C/W).
T_{hl}	Rectified line period (s)
T_s	Switchng period of the primary switch (s).
V_{acp}	Peak voltage value of the utility grid (V).
V_d	Diode forward voltage (V).
V_{dc}	Input voltage (V).
$V_{\mathrm{dc,max}}$	Maximum input voltage at which the inverter can deliver its rated power under MPPT conditions (V).
$V_{\mathrm{dc,min}}$	Minimum input voltage at which the inverter can deliver its rated power under MPPT conditions (V).
V_e	Effective core volume (mm^3).
$V_{\mathrm{sp},i}$	Peak voltage value on the main MOSFET for each switching cycle i (V).
$V_{\mathrm{tr,BD}}$	Breakdown voltage of the secondary transformer side switches (V).
$V_{\mathrm{tr,pri,BD}}$	Breakdown voltage of the transistor on the primary transformer side (V).
$V_{\mathrm{tr,pri,max}}$	Maximum voltage on the transistor on the primary transformer side (V).
$V_{\mathrm{tr,sec,BD}}$	Breakdown voltage of the transistors on the secondary transformer side (V).
$V_{\mathrm{tr,sec,max}}$	Maximum voltage on the transistors on the secondary transformer side (V).

I. INTRODUCTION

IN THE last two decades it has become more and more obvious that the rapid climate changes and the energy dead end of fossil fuel dependence accelerate the large-scale adoption of clean energy sources. Toward this aim, the higher interest is concentrated in solar and wind energy exploitation. Nowadays, PV power injection to the utility grid is gaining more and more admittance [1], [2]. The latest technology on decentralized grid-connected PV systems is the ac–PV module [2]–[7], which is the integration of the PV module and the inverter into a single unit that operates as an ac generator. This configuration promises optimum MPPT operation unaffected by shadows that can remarkably decrease the total power generation. The ac–PV module can be easily installed to any rooftop without any special technical knowledge or extreme safety precautions. Furthermore, its modular layout assures effortless enlargement of the installations when desired.

The power converter unit of an ac–PV module is usually a single-phase inverter, ranging from 50 to 400 W. There are many single or multistage topologies about grid-connected inverters for PV modules in the international bibliography [2]. In any case, all topologies must be characterized by high efficiency, high power density, low volume, and extreme reliability.

The flyback topology [6]–[8] concentrates on the aforementioned requirements and many more advantages, forming an attractive selection for the ac–PV module converter. Therefore, special effort has been given to improve its reliability, cost, and efficiency by judiciously selecting the design parameters and/or by adopting different control techniques [6]–[8]. However, except some well-known and widely used common practices and empirical rules [7], there are no specific directions or analytically verified guidelines to clarify the relation between this parameters selection and efficiency.

In this paper, a special effort was given to comprehend this correlation and form a methodology that clearly defines, always in accordance with the required specifications, the values of the design parameters in order to maximize an objective function that is the weighted efficiency. To perform this task, the flyback inverter is analyzed, power losses on each component are estimated, and an algorithm is established to accurately define the appropriate parameters.

II. FLYBACK CONVERTER IN DISCONTINUOUS CONDUCTION MODE OPERATION AS A GRID-CONNECTED CURRENT SOURCE INVERTER

The flyback inverter, as shown in Fig. 1, performs energy flow from the dc to the ac side, by using two identical secondary windings. Each of them is able to transfer energy to the ac side during a utility grid half cycle. For this reason, a semiconductor switch is placed in each secondary winding, and is appropriately controlled by the mains polarity.
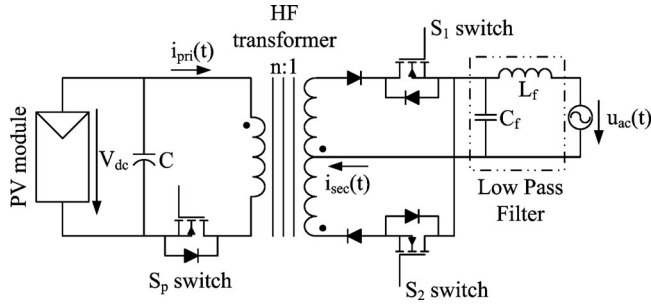
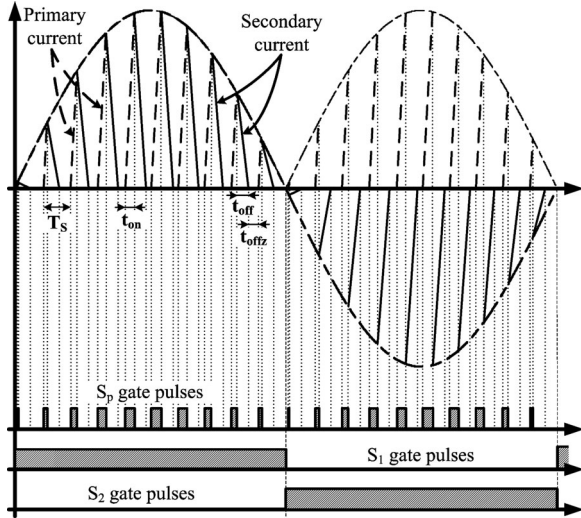Fig. 1. Flyback inverter topology diagram.

Fig. 2. Current waveforms and switching sequence diagram.

Therefore, while the main semiconductor S_p is modulated in HF (20–200 kHz), the switches of the secondary winding are modulated in 50 or 60 Hz. The switching sequence of each semiconductor can be observed in Fig. 2. In the following analysis, only discontinuous conduction mode (DCM) is considered due to its simplicity of control. A thorough analysis of the flyback inverter is described in [7]. The transferred power is expressed by the following:

$$P_{\mathrm{PV}} = \frac{1}{4} V_{\mathrm{dc}}^2 g_L d_p^2 \qquad (1)$$

where

$$g_L = \frac{1}{L_1 f_s}. \qquad (2)$$

III. DESIGN METHODOLOGY AND PERFORMANCE OPTIMIZATION

The ac–PV module has to ensure the maximum exploitation of the solar energy. Therefore, the efficiency of the inverter has to be high, not only for the nominal power, but also for other power values corresponding to various irradiance levels. To overcome this obstacle, the European weighted-efficiency η_{EUR} [9], given by (3), and the American weighted-efficiency

η_{CEC} [9], given by (4), can be used. These factors, depending on the PV installation location, integrate in one quantity the efficiency at various power levels

$$\eta_{\mathrm{EUR}} = 0.03\eta_{5\%} + 0.06\eta_{10\%} + 0.13\eta_{20\%}$$
$$+ 0.10\eta_{30\%} + 0.48\eta_{50\%} + 0.20\eta_{100\%} \qquad (3)$$

$$\eta_{\mathrm{CEC}} = 0.04\eta_{10\%} + 0.05\eta_{20\%} + 0.12\eta_{30\%}$$
$$+ 0.21\eta_{50\%} + 0.53\eta_{75\%} + 0.05\eta_{100\%} \qquad (4)$$

where η_w is the efficiency at a specified PV power level $P_{\mathrm{PV},w}$ given as a percentage of the nominal power $P_{\mathrm{PV,nom}}$ of the PV module. Therefore

$$w\,(\%) = \frac{P_{\mathrm{PV},w}}{P_{\mathrm{PV,nom}}} 100 \qquad (5)$$

$$\eta_w = 1 - \frac{P_{\mathrm{loss},w}}{P_{\mathrm{PV},w}} = 1 - r_{\mathrm{loss},w} \qquad (6)$$

where $P_{\mathrm{loss},w}$ are the inverter losses at the specified power level.

The basic aim of this paper is to establish a methodology based on the weighted-efficiency optimization to accurately define all the design parameters of the topology. This task requires inverter losses calculation at different power levels. However, power losses depend on many parameters that correlate directly to the topology components as well as to various operational variables. In order to establish the optimization algorithm, it is necessary to clearly define the design parameters and the dependent variables. For this reason, all system parameters are reported in Table I and classified in three different categories, namely, the input specifications, the component parameters, and the performance parameters. As it is shown in Table I, the system parameters are numerous; therefore, special manipulations must be conducted in order to make specific and proper conclusions.

The inverter under optimization should be able to deliver its rated power $P_{\mathrm{PV,nom}}$ under MPPT conditions for different input voltage levels that fluctuate between $V_{\mathrm{dc,min}}$ and $V_{\mathrm{dc,max}}$ [9]. Therefore, the efficiency maximization procedure has to take into consideration the input voltage limits. In order to meet this goal, the algorithm optimizes the design for the minimum voltage, a fact that composes the worst-case scenario regarding the efficiency. The aim of this paper is not to evaluate the MPPT performance of the inverter, but the efficiency of the power circuit. Therefore, during the experimental procedure, the MPPT algorithm is disabled as it is defined by the international standard [9].

At the first step of the optimization procedure, the input parameters have to be assigned. These parameters are determined by the PV module characteristics and the utility grid specifications.

At the second step, the packages and the technology of the main and the secondary switches must be selected. According to these selections, the following parameters can be determined: $t_{f,\mathrm{pri}}$, the relation between R_{ds} and the transistor breakdown voltage $V_{\mathrm{tr,BD}}$, as well as the V_d. Due to the operation of the inverter (DCM), the variables $t_{r,\mathrm{pri}}$, $t_{r,\mathrm{sec}}$, $t_{f,\mathrm{sec}}$, and R_d can be neglected. In fact, the primary transformer side transistor is switched ON at zero current, the secondary transformer side

TABLE I
PARAMETERS OF THE SYSTEM

Input and Output Specifications			$P_{PV,nom}$, $V_{dc,min}$, $V_{dc,max}$, V_{acp}	input and output electrical characteristics of the inverter
Component Parameters	Semiconductors Parameters	Primary side Mosfet	$R_{ds,pri}$, $t_{f,pri}$, $t_{r,pri}$, $V_{DSBD,pri}$	on-resistance, rise and fall time, breakdown voltage
		Secondary side Mosfets	$R_{ds,sec}$, $t_{f,sec}$, $t_{r,sec}$, $V_{DSBD,sec}$	
		Secondary side Diode	V_d, R_d	forward voltage drop, series resistance of the diode
	Transformer parameters	Core Type	A_w, V_e, A_e, l_e, R_t, l_g	window area, volume, cross sectional area, effective length, thermal resistance from the external ambient to the central hot spot, air gap length
		Core Material	α, β, k, B_{sat}	material coefficients from material datasheet, saturation flux density
		Winding Parameters	r, str_{pri}, str_{sec}, J, N_{pri}, n, $C_{ff}=A_{w,Cu}/A_w$	wire radius, strands of the primary and secondary winding, current density, turns ratio, copper fill factor
Performance Parameters			n, f_s, J, B_p	parameters judicioucly extracted from the optimization algorithm in order to maximize efficiency
Objective Function			$\eta_{Weighted}=f(n,f_s,J,B_p)$	the objective function is the weighted efficiency defined by the CEC or European standards
Constraints			DT_{max}, $d_{p,max}$, $V_{tr,BD,max}$, B_{sat}, $C_{ff,max}$	constraints that ensure feasibility and proper operation of the design
Design Parameters			f_s, n, N_{pri}, str_{pri}, str_{sec}, l_g, Core type, Core material, Mosfet types, Diode	parameters needed to implement the system

transistors are switched ON at almost zero voltage and switched OFF at zero current, and the secondary current is small enough so that resistive losses at the diodes can be neglected.

The leakage inductance of the transformer contributes to the system power loss because all its energy is dissipated on the passive snubber of the primary switch. The passive snubber consists of a common cathode diode and a zener diode. The leakage inductance of laboratory prototypes ranges from 0.5% to 3% of the primary inductance. Therefore, in order to make accurate loss estimation, a power loss ratio due to the leakage inductance of 2.5% is integrated to the optimization algorithm.

Afterward, when all the aforementioned parameters are defined, the optimization algorithm is executed taking into consideration every core type from a core database.

The optimization algorithm deduce the design parameters for each core type and the final selection will correspond to the core that gives the absolutely best weighted efficiency in respect to the operational constraints.

Therefore, at the third step, giving the type and the material of the core, all corresponding manufacturer parameters can be defined.

Following the previously analyzed procedure, the independent variables are now reduced to only four that are reported in Table I as performance parameters. Furthermore, the optimization procedure has to ensure the feasibility and the proper operation of the proposed design.

In order to fulfill such a task, the constraints presented in Table I should be applied. These limitations consist of: the maximum voltage on the secondary switches (7) [7], the maximum temperature rise of the magnetic component (8) [12], the duty cycle limitation (9) [7] to ensure DCM operation, the copper fill factor of the core window (10) [12], and the maximum flux density in order to avoid saturation (11)

$$V_{\mathrm{tr,sec,max}}(n) = \left(\frac{(V_{\mathrm{dc,max}}/0.8)}{nV_{\mathrm{acp}}} + 2 \right) V_{\mathrm{acp}}130\% \leq V_{\mathrm{tr,BD}} \tag{7}$$

$$DT(n, V_{\mathrm{dc}}, f_s, B_p, J, r) = R_t \left[P_{\mathrm{CRL}}(n, V_{\mathrm{dc}}, f_s, B_p) + P_{\mathrm{CPL}}(n, V_{\mathrm{dc}}, f_s, B_p, J, r) \right] \leq DT_{\max} \tag{8}$$

$$d_p \leq d_{p\max} = \left(\frac{V_{\mathrm{dc,min}}}{nV_{\mathrm{acp}}} + 1 \right)^{-1} \tag{9}$$

$$C_{ff}(n, V_{\mathrm{dc}}, f_s, B_p, J, r) = \frac{A_{w,\mathrm{Cu}}(n, V_{\mathrm{dc}}, f_s, B_p, J, r)}{A_w} \leq C_{ff\max} \tag{10}$$

$$B_p \leq B_{\mathrm{sat}}. \tag{11}$$

The semiconductors on the secondary transformer side are under severe voltage stress due to the high V_{acp} and the reflection of the input voltage to the secondary. In order to increase reliability, the approximate equation proposed in [7] that estimates the maximum voltage on the secondary's switches is by 30% oversized to handle not only the steady state voltage, but also transistion voltage stress [10], [11]. Furthermore, we can assume that $V_{dc,max}$ is 80% of the open-circuit voltage V_{oc} of the PV module.

Transformer loss is mainly limited by a maximum hot spot temperature rise at the core surface. As it is described by (8), the temperature rise is proportional to the power loss and the thermal resistance R_t between the external ambient to the central hot spot. Both the copper and core loss contribute to the transformer temperature rise. Transformer temperature rise is examined under worst-case conditions in which the power losses are at their peak and the input power is the highest.

The copper fill factor for economical transformer design (ETD) cores using high-voltage insulation litz wire and random layered coil is approximately 0.35 [12].

Taking into consideration these constraints and by reducing the multidimensional parameter space, the design procedure becomes the optimization of an objective function—the weighted efficiency—that depends on only four variables, the performance parameters. Furthermore, the constraints limit even more the possible configurations. To resolve this mathematical problem, a numerical algorithm for constrained nonlinear global optimization is adopted and implemented on a software platform [13]. In order to formulate the equations to predict the converter losses, the rms and average value of both input and output currents should be calculated. The adequate equations are presented in the following paragraphs.

IV. INPUT AND OUTPUT CURRENT CALCULATION

At first, the current of the primary winding is examined and the necessary equations are presented.

The instant current of the primary winding is given by the following [7]:

$$i_{pri}(t_i) = \frac{V_{dc}}{L_1} t_i, \qquad 0 < t_i < t_{ON,i} \tag{12}$$

where the subindex i indicates every counting (switching) cycle.

Therefore, the peak current $I_{pri,p,i}$ at each switching cycle is the current value at the end of each ON-time interval and is given by:

$$I_{pri,p,i} = \frac{V_{dc}}{L_1} t_{ON,i}. \tag{13}$$

For the inverter to inject active power to the grid, the peak currents of the primary transformer side outline a sinusoidal waveform (see Fig. 2). For this reason and by taking into consideration (13), it can be concluded that the time interval $t_{ON,i}$, in which the main Mosfet conducts, has sinusoidal form and is described by

$$t_{ON} = T_s d_p \sin(\omega t) \Rightarrow t_{ON,i} = T_s d_p \sin\left(\frac{\pi}{m} i\right) \tag{14}$$

where m is the integer part of T_{hl}/T_s.

In [7], the average current value is described as follows:

$$I_{pri,avg} = \frac{1}{4} \frac{V_{dc} T_s d_p^2}{L_1}. \tag{15}$$

The rms current value of the primary winding can be found from the following equation:

$$I_{pri,rms}^2 = \left(\sqrt{\frac{1}{T_{hl}} \int_0^{T_{hl}} i_{pri}^2(t) dt} \right)^2 = \frac{1}{T_{hl}} \int_0^{T_{hl}} i_{pri}^2(t) dt$$

$$= \frac{1}{T_{hl}} \left[\int_0^{T_s} i_{pri}^2(t) dt + \int_{T_s}^{2T_s} i_{pri}^2(t) dt \right.$$

$$\left. + \cdots \int_{(m-1)T_s}^{mT_s} i_{pri}^2(t) dt + Q \right]$$

$$= \frac{1}{T_{hl}} \left[\sum_{i=1}^m \int_{(i-1)T_s}^{iT_s} i_{pri}^2(t) dt + Q \right] \tag{16}$$

where Q is the rest part of the integral—referring to the beginning or to the ending of a line cycle—and since $T_{hl} \gg T_s$ it can be neglected.

Taking into consideration (12), this integral can be calculated as follows:

$$\int_{(i-1)T_s}^{iT_s} i_{pri}^2(t) dt = \int_0^{t_{ON,i}} i_{pri}^2(t_i) dt = \left[\frac{V_{dc}}{L_1} \frac{t_i^2}{2} \right]\Big|_0^{t_{ON,i}}$$

$$= \left[\frac{V_{dc}}{L_1} \right]^2 \frac{t_{ON,i}^3}{3}. \tag{17}$$

By combining (14), (16), and (17), and after some mathematical manipulations (see Appendix A), we conclude that the following:

$$I_{pri,rms}^2 = \frac{V_{dc}^2 T_s^2 d_p^3}{3L_1^2} \left[\frac{1}{m} \sum_{i=1}^m \sin^3\left(\frac{\pi}{m} i\right) \right] \approx \frac{4}{9\pi} \frac{V_{dc}^2 T_s^2 d_p^3}{L_1^2}. \tag{18}$$

In order to calculate the current values of the secondary winding, the same procedure can be executed.

The instant current of the secondary winding is given by

$$i_{sec}(t_i) = n I_{pri,p,i} \left(1 - \frac{t_i}{t_{off}} \right), \qquad 0 < t_i < t_{OFF} \tag{19}$$

and the time interval during which each secondary conducts is constant [7] and is given by

$$t_{OFF} = \frac{V_{dc} T_s d_p}{n V_{acp}}. \tag{20}$$

The average current value of each secondary winding can be extracted by the following equation:

$$I_{sec,avg} = \frac{1}{2T_{hl}} \int_0^{T_{hl}} i_{sec}(t) dt = \frac{1}{2T_{hl}} \left[\int_0^{T_s} i_{sec}(t) dt \right.$$

$$\left. + \int_{T_s}^{2T_s} i_{sec}(t) dt + \cdots \int_{(m-1)T_s}^{mT_s} i_{sec}(t) dt + Q \right]$$

$$= \frac{1}{2T_{hl}} \left[\sum_{i=1}^m \int_{(i-1)T_s}^{iT_s} i_{sec}(t) dt + Q \right]. \tag{21}$$

The semiconductors on the secondary transformer side conduct sequentially, each one for half period of the utility voltage. Therefore, the current should be calculated for the entire period of the utility voltage that is equal to $2T_{hl}$.

Taking into consideration (19), the integral of (21) can be calculated as follows:

$$\int_{(i-1)T_s}^{iT_s} i_{\rm sec}(t)dt = \int_0^{t_{\rm OFF}} i_{\rm sec}(t_i)dt$$

$$= nI_{{\rm pri},p,i}\left[\left(t_i - \frac{t_i^2}{2t_{\rm OFF}}\right)\right]\Big|_0^{t_{\rm OFF}}$$

$$= \frac{nI_{{\rm pri},p,i}t_{\rm OFF}}{2}. \tag{22}$$

By combining (13), (14), (20), (21), and (22), by neglecting the term Q, and after some mathematical manipulations (see Appendix A), we can conclude that

$$I_{\rm sec,avg} = \frac{V_{\rm dc}^2 T_s d_p^2}{4V_{\rm acp}L_1}\left[\frac{1}{m}\sum_{i=1}^{m}\sin\left(\frac{\pi}{m}i\right)\right] = \frac{1}{2}\frac{1}{V_{\rm acp}\pi}\frac{V_{\rm dc}^2 T_s d_p^2}{L_1}. \tag{23}$$

The rms current value of each secondary winding is given by the equations

$$I_{\rm sec,rms}^2 = \left(\sqrt{\frac{1}{2T_{hl}}\int_0^{T_{hl}} i_{\rm sec}^2(t)dt}\right)^2 = \frac{1}{2T_{hl}}\int_0^{T_{hl}} i_{\rm sec}^2(t)dt$$

$$= \frac{1}{2T_{hl}}\left[\int_0^{T_s} i_{\rm sec}^2(t)dt + \int_{T_s}^{2T_s} i_{\rm sec}^2(t)dt\right.$$

$$+ \cdots \int_{(m-1)T_s}^{mT_s} i_{\rm sec}^2(t)dt + Q\right]$$

$$= \frac{1}{2T_{hl}}\left[\sum_{i=1}^{m}\int_{(i-1)T_s}^{iT_s} i_{\rm sec}^2(t)dt + Q\right]. \tag{24}$$

Taking into consideration (19), the integral of (24) can be calculated as follows:

$$\int_{(i-1)T_s}^{iT_s} i_{\rm sec}^2(t)dt = \int_0^{t_{\rm OFF}} i_{\rm sec}^2(t_i)dt = \left[nI_{{\rm pri},p,i}\right]^2$$

$$\cdot\left[t_i - 2\frac{t_i^2}{2t_{\rm OFF}} + \frac{t_i^3}{3t_{\rm OFF}^2}\right]\Big|_0^{t_{\rm OFF}}$$

$$= \frac{\left[nI_{{\rm pri},p,i}\right]^2 t_{\rm OFF}}{3}. \tag{25}$$

By combining (13), (14), (20), (24), and (25), by neglecting the term Q, and after some mathematical manipulations (see Appendix B), we can conclude that the following:

$$I_{\rm sec,rms}^2 = \frac{nV_{\rm dc}^3 T_s^2 d_p^3}{6V_{\rm acp}L_1^2}\left[\frac{1}{m}\sum_{i=1}^{w}\sin^2\left(\frac{\pi}{m}i\right)\right] = \frac{n}{12V_{\rm acp}}\frac{V_{\rm dc}^3 T_s^2 d_p^3}{L_1^2}. \tag{26}$$

The loss calculation procedure of the individual components is based on the calculated currents. This analysis is divided into two categories: 1) the semiconductors loss calculation and 2) the transformer loss calculation.

V. CALCULATION OF SEMICONDUCTOR LOSSES

The semiconductor losses can be distinguished in switching and conduction losses.

A. Switching Losses

Due to the DCM operation in the primary transformer side, there are semiconductor switching losses only during the turn-OFF transition, whereas the switching losses on the semiconductors of the secondary transformer side can be neglected since the transistors are switched ON at zero voltage and switched OFF at zero current.

In order to compute the total switching losses, the energy lost in each switching cycle is firstly calculated by the following equation:

$$E_i = \frac{V_{{\rm sp},i}\cdot I_{{\rm sp},i}}{2}t_{f,{\rm pri}} = \frac{V_{{\rm sp},i}I_{{\rm pri},p,i}}{2}t_{f,{\rm pri}}. \tag{27}$$

Since the switching frequency is much higher than the frequency of the grid, we can assume that the voltage during the switching time remains constant and is equal to

$$V_{{\rm sp},i} = V_{\rm dc} + nV_{{\rm ac},i} = V_{\rm dc} + nV_{\rm acp}\sin\left(\frac{\pi}{m}i\right). \tag{28}$$

By combining (13), (14), and (28), (27) can be rewritten as follows:

$$E_i = \frac{t_{f,{\rm pri}}V_{\rm dc}T_s d_p}{2L_1}\left[V_{\rm dc}\sin\left(\frac{\pi}{m}i\right) + nV_{\rm acp}\sin^2\left(\frac{\pi}{m}i\right)\right]. \tag{29}$$

In order to calculate the power loss for a time period of T_{hl}, we can write

$$P_{\rm SL,pri} = \frac{1}{T_{hl}}\sum_{i=1}^{m} E_i \tag{30}$$

$$P_{\rm SL,pri} = \frac{t_{f,{\rm pri}}V_{\rm dc}d_p}{2L_1}$$

$$\times\left[V_{\rm dc}\frac{1}{m}\sum_{i=1}^{m}\sin\left(\frac{\pi}{m}i\right) + nV_{\rm acp}\frac{1}{m}\sum_{i=1}^{m}\sin^2\left(\frac{\pi}{m}i\right)\right]. \tag{31}$$

After the series computation (see Appendixes A and B), and by combining (31) and (1), the power switching loss ratio appears

$$\frac{P_{\rm SL,pri}(n,w,V_{\rm dc},f_s)}{P_{\rm PV,w}} = \frac{f_s t_{f,{\rm pri}}\left((nV_{\rm acp}/V_{\rm dc}) + (4/\pi)\right)}{d_p(n,w,V_{\rm dc})}. \tag{32}$$

In (32), the parasitic output capacitor loss is absent because latest research presented in [14] proved that this kind of loss is already integrated in (27).

B. Conduction Losses

As it concerns the conduction losses ($P_{\rm CL,pri}$ and $P_{\rm CL,sec}$ on the switches in primary and secondary transformer side,
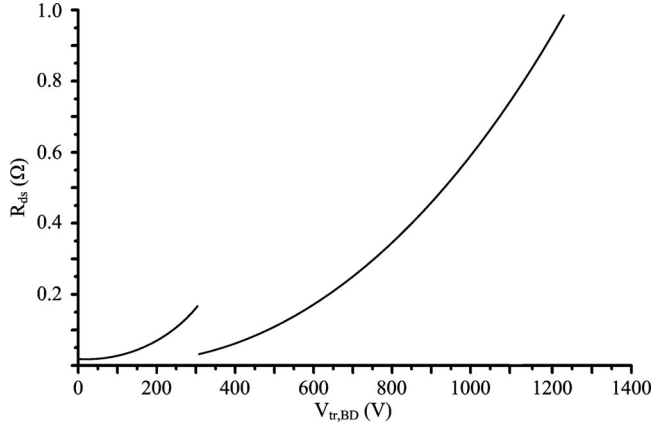
Fig. 3. Relation between the ON-resistance and the semiconductor breakdown voltage at 100 °C.

respectively), they can be described as follows:

$$P_{\mathrm{CL,pri}} = I_{\mathrm{pri,rms}}^2 R_{\mathrm{ds,pri}} \tag{33}$$

$$P_{\mathrm{CL,sec}} = 2 \cdot I_{\mathrm{sec,rms}}^2 R_{\mathrm{ds,sec}}. \tag{34}$$

In (34), the total conduction losses on both the secondary switches are presented. The problem that came up was the estimation of the ON-resistance of the appropriate MOSFET. As the transformer ratio changes, the maximum voltage on the semiconductor switches varies, leading to different MOSFET type with different ON-resistance value. In order to introduce this variation into the optimization algorithm, the relation between the ON-resistance and the transistor breakdown voltage mentioned in [15] is used. To meet our requirements, this relationship was adjusted to match the datasheet characteristics of a single MOSFET manufacturer. The collected data are approximated, using curve fitting techniques, by two different curves, depending on the transistor breakdown voltage range, as shown in Fig. 3. Therefore, we can write

$$R_{\mathrm{ds,ON}} = k_1 \left[V_{\mathrm{tr,BD}} \right]^{k_2} + k_3 \tag{35}$$

where $k_1 = 10.58 \cdot 10^{-8}$, $k_2 = 2.48$, and $k_3 = 0.033$ for the lower breakdown voltage range at 100 °C, and $k_1 = 3.796 \cdot 10^{-8}$, $k_2 = 2.4$, and $k_3 = 0$ for the higher breakdown voltage range at 100 °C.

The next step is to express the ON-resistance as a function of the inverter design parameters. This is accomplished by replacing the $V_{\mathrm{tr,BD}}$ by the appropriate (36) and (37) that gives the maximum voltage across each transistor [7]

$$V_{\mathrm{tr,pri,BD}} = 1.3 V_{\mathrm{tr,pri,max}} = 1.3 \left(\left(\frac{V_{\mathrm{dc,max}}}{0.8} \right) + n V_{\mathrm{ac}p} \right) \tag{36}$$

$$V_{\mathrm{tr,sec,BD}} = 1.3 V_{\mathrm{tr,sec,max}} = 1.3 \left(\frac{(V_{\mathrm{dc,max}}/0.8)}{n} + 2 V_{\mathrm{ac}p} \right). \tag{37}$$

Finally by combining (18), (26), (33), (34), (35), (36), (37), and (1), we conclude that the conduction losses ratio can be expressed by (38) and (39)

$$\frac{P_{\mathrm{CL,pri}}(n, w, V_{\mathrm{dc}})}{P_{\mathrm{PV},w}} = \frac{16 g_L(n) R_{\mathrm{ds,pri}}(n) d_p(n, w, V_{\mathrm{dc}})}{9\pi} \tag{38}$$

$$\frac{P_{\mathrm{CL,sec}}(n, w, V_{\mathrm{dc}})}{P_{\mathrm{PV},w}} = \frac{2 n V_{\mathrm{dc}} g_L(n) R_{\mathrm{ds,sec}}(n) d_p(n, w, V_{\mathrm{dc}})}{3 V_{\mathrm{ac}p}}. \tag{39}$$

The diode conduction losses can be calculated by multiplying the average current (23) by the diode voltage drop V_d forming the power loss ratio that is given by (40). Because there are two diodes on the secondary side, the diode conduction losses are doubled

$$\frac{P_d}{P_{\mathrm{PV},w}} = 2 \left(\frac{2 V_d}{\pi V_{\mathrm{ac}p}} \right) = \frac{4 V_d}{\pi V_{\mathrm{ac}p}}. \tag{40}$$

VI. TRANSFORMER LOSS CALCULATION

The losses on the magnetic element are highly related not only to the parameters of its construction, but also to the waveform of the flowing current. There are many different approaches to predict the magnetic losses, but the most fundamental step is the discrimination between core and copper losses. The core losses deal with the material and size of the core, temperature, frequency, and form of the flux waveforms. On the other hand, the copper losses relate to skin and proximity effects of the windings.

A. Core Loss Estimation for Arbitrary Waveforms

Aiming for high efficiency, the modern, HF, circuit topologies are characterized by nonnegligible core losses. A compromise between miniaturization and efficiency seems unavoidable, and thus an accurate core loss prediction should take place. In power electronics, this task is difficult because the magnetic material is exposed to nonsinusoidal flux waveforms. Significant research about magnetic materials has been conducted for many years but the most fundamental loss equations have been formulated for sinusoidal excitations and processes. Only in the last two decades, a lot of effort was given to extract formulas that estimate core losses under arbitrary flux waveforms. In this paper, a core loss estimation formula is adopted that is not only accurate, but also practical and simple to be integrated into the optimization algorithm.

In the international bibliography, there are two main paths to predict core losses. The first one is to comprehend the physical procedures, approach that mainly concerns material scientists, while the second one is some kind of macroscopic estimation approach that mainly concerns electrical engineers. As it is clearly pointed out in [16], the rather chaotic time and space distribution of the magnetization changes cannot be described exactly, therefore, a practical means of calculating losses cannot be provided. Taking this into consideration, the adopted formula was selected along the path of the macroscopic and empirical approach that can be subdivided into hysteresis models, loss separation, and empirical formulas.

1) Hysteresis Models: The hysteresis models describe mathematically the hysteresis loop and determine the core losses in each switching cycle. There are many different approaches about the hysteresis models with the most fundamental those of Preisach [17] and Jiles and Atherton [18]. The models by Preisach, and Jiles and Atherton are based on physical models. Both of these models describe that the static behavior of the magnetic materials and subsequent improvements [19] were necessary in order to integrate the dynamic behavior and improve the accuracy. Another behavioral model of magnetic materials is presented in [20]. This model takes into account both hysteresis and dynamic phenomena. The results obtained are very satisfactory but pieces of experimental data are needed to identify its parameters. As it is clearly mentioned in [16] and [21], hysteresis models have some drawbacks that make their use impractical. First, the parameters of the models are not provided by the manufacturers of the magnetic materials. Second, both Preisach and Jiles–Atherton models as well as their improvements have limited practical use due to the high number of empirical parameters required.

2) Core Loss Based on Loss Separation: Another remarkable core loss estimation method is by discriminating the core losses into three parts, namely, static hysteresis loss P_h, the classical eddy losses P_{cl}, and excess or anomalous eddy losses P_{ex}. The hysteresis losses are given from the hysteresis loop area; therefore, they depend on the peak flux density and are proportional to the frequency. The classical eddy losses are generated from the eddy current that flows through the core body. They depend on the cross-section area of the core and the resistivity of the material. Finally, the excess or anomalous eddy current losses describe the phenomenon of the nonuniform change in the magnetic field due to the domain walls motion. A thorough description of the loss separation approach and a comprehensive analysis of the eddy losses origins are presented in [22]. The most significant drawback in loss separation core loss approach is that only the classical eddy losses can be calculated. The hysteresis losses and excess eddy current losses have to be determined experimentally. As it is discussed in [23], these approaches require extensive measurement and parameter extraction with a given material before they become useful. Some parameters are extracted by comparing measurements under sinusoidal excitation with the results of the calculating formulas. Finally, as it is mentioned in [22], the resistivity supplied by the manufacturer is not very accurate and can even vary significantly with the frequency. Also, in the same paper, the parameter that characterizes the statistical distribution of the local coercive fields demands a lot of effort to be obtained.

3) Empirical Formulas: Both the hysteresis and loss separation approaches may present accurate estimations, but they present impractical application when experimental data are absent. The last core loss prediction approach is based on empirical equations. The most widely known empirical equation is the so-called Steinmetz equation $P_{cl} = k f^\alpha \hat{B}^\beta$, where P_{cl} is the time average power loss per unit volume, $\hat{B}$ is the peak flux amplitude, and f is the frequency of the sinusoidal excitation. The k, α, and β are the three empirical parameters whose value depend on frequency, temperature, and material.

Concerning the Steinmetz equation, the empirical parameters and the data provided by the manufacturers of magnetic materials are valid only for sinusoidal excitation; a fact that prevents their use in topologies with different excitation waveforms and thus to the flyback transformer.

Therefore, in order to apply the Steinmetz Equation over nonsinusoidal waveforms, Fourier expansion could be used. Though, due to the high nonlinearity core losses dependence over frequency and flux density, the confidence for reliable estimation over a wide range of different waveform excitation is limited. Seeking a more practical and universal approach capable to estimate core loss for arbitrary waveshapes, the modified Steinmetz equation (MSE), the generalized Steinmetz equation (GSE), and the improved GSE (iGSE) were examined. All these approaches are based on the Steinmetz equation recognizing its importance due to not only its high accuracy and practical use, but also because that the three empirical parameters are always supplied by the material's manufacturer.

The MSE is presented in [16] and is the first empirical equation that is consistent with Steinmetz equation and can be used to calculate core losses for nonsinusoidal excitations. The idea is that the core losses depend on the remagnetization rate dM/dt and hence to the rate of flux density derivative dB/dt. As it is mentioned in [16], the MSE describes the physical origin of the losses and gives the opportunity to calculate the core losses in the time domain for arbitrary shapes of inductions. Compared with the Steinmetz equation, no additional parameters are needed. The MSE seems to meet the requirements for the flyback transformer application in DCM operation.

In [23], GSE is presented. The writers succeeded to avoid the anomalies of the MSE by defining the losses in relation to the flux density derivative dB/dt, instantaneous value $B(t)$, and its overall waveform.

In [24], the iGSE is presented. The writers replaced the power loss dependence on the instantaneous B with that of peak-to-peak flux density ΔB and formulated (41). Another crucial improvement that increases the iGSE range of application is the addition of the minor loop separation algorithm. The estimation equations are applied to every distinguished minor loop of the arbitrary waveforms. The flyback transformer excitation under DCM control scheme does not contain any minor loops, but the availability of such an option is a strong capability for any future control strategy improvement that generates new excitation conditions.

The core losses during a switching period of any arbitrary waveform are given by

$$P_{\text{CoreLosses}} = V_e \frac{k_f (\Delta B)^{\beta - \alpha}}{T} \sum_j \left| \frac{V_j}{N_{\text{pri}} A_e} \right|^\alpha (\Delta t_j) \quad (41)$$

where

$$k_f = \frac{k}{2^{\beta+1} \pi^{\alpha-1} (0.2761 + (1.7061/\alpha + 1.354))}. \quad (42)$$
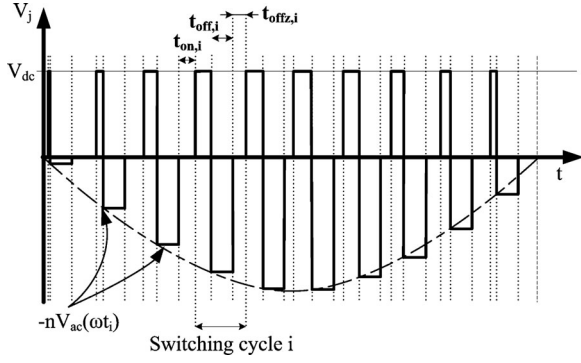
Fig. 4. Voltage across the HF transformer.

B. Core Loss Calculation of the Flyback Inverter

The excitation of the flyback transformer under DCM is described by (43) and presented in Fig. 4. When S_p switch conducts, the voltage on the transformer primary winding is $V_{\rm dc}$ and by the time it switches OFF the voltage on the transformer is that of the grid

$$V_j(t_i) = \begin{cases} V_{\rm dc}, & t_i < t_{{\rm ON},i} \\ -nV_{\rm ac}(\omega t_i), & t_{{\rm ON},i} < t_i < t_{{\rm OFF},i} \\ 0, & t_{{\rm OFF},i} < t_i < t_{{\rm OFF}z,i} \end{cases}. \quad (43)$$

The flux swing during each switching cycle is calculated from the Faraday's Law and is given by:

$$\Delta B_i = \frac{V_{\rm dc} t_{{\rm ON},i}}{N_{\rm pri} A_e}. \quad (44)$$

The core loss for each switching cycle (45) is extracted by combining (41) with (14), (20), (43), and (44)

$$P_{{\rm CRL},i} = V_e \frac{k_f V_{\rm dc}^{\beta-\alpha}}{(N_{\rm pri} A_e)^\beta} T_s^{\beta-\alpha+1} d_p^{\beta-\alpha+1} \left[V_{\rm dc}^\alpha \left[\sin\left(\frac{\pi}{m} i\right) \right]^{\beta-\alpha+1} \right.$$
$$\left. + V_{\rm acp}^{\alpha-1} n^{\alpha-1} V_{\rm dc} \left[\sin\left(\frac{\pi}{m} i\right) \right]^\beta \right]. \quad (45)$$

For a time interval equal to T_{hl}, a series of successive core losses takes place. The total power core loss (47) is estimated by analytically computing a series of losses (46)

$$P_{\rm CRL} = \frac{1}{T_{hl}} \sum_{i=1}^m T_s P_{{\rm CRL},i} \quad (46)$$

$$P_{\rm CRL} = V_e \frac{k_f V_{\rm dc}^{\beta-\alpha}}{(N_{\rm pri} A_e)^\beta} T_s^{\beta-\alpha} d_p^{\beta-\alpha+1}$$
$$\times \left[V_{\rm dc}^\alpha \frac{1}{m} \sum_{i=1}^m \left[\sin\left(\frac{\pi}{m} i\right) \right]^{\beta-\alpha+1} \right.$$
$$\left. + V_{\rm acp}^{\alpha-1} n^{\alpha-1} V_{\rm dc} \frac{1}{m} \sum_{i=1}^m \left[\sin\left(\frac{\pi}{m} i\right) \right]^\beta \right]. \quad (47)$$

Through extensive curve fitting and linear approximation for simplicity, it can be concluded that the series calculation of (47)

can be executed for various exponents according to (48)

$$\frac{1}{m} \sum_{i=1}^m \left[\sin\left(\frac{\pi}{m} i\right) \right]^u = 0.67 - 0.083u, \quad u \in [1.7, 3.2] - \{\mathbb{Z}\}$$
$$(48)$$

$$\frac{P_{\rm CRL}(n, w, V_{\rm dc}, f_s, B_p)}{P_{{\rm PV},w}}$$
$$= V_e \frac{k_f V_{\rm dc}^{\beta-\alpha+1}}{(N_{\rm pri} A_e)^\beta} \frac{T_s^{\beta-\alpha} d_p^{\beta-\alpha+1}(n, w, V_{\rm dc})}{P_{{\rm PV},w}}$$
$$\times \left(V_{\rm dc}^{\alpha-1} 0.51762 + V_{\rm acp}^{\alpha-1} n^{\alpha-1} 0.46 \right). \quad (49)$$

It can be easily understood that the core loss ratio (49) depends on the turns ratio n, input power level w, input voltage $V_{\rm dc}$, switching frequency f_s, and peak flux density B_p.

C. Copper Losses Estimation of the Multiwinding HF Transformer

The copper losses that increase the magnetic component temperature and winding resistance lead to special operation conditions and decrease the overall performance. Both proximity and skin effect influence copper losses. A semiempirical model to determine HF copper losses for nonlayered coils is presented in [25].

The HF current through the flyback transformer obligates the use of significantly low diameter copper wire; a fact that proves the implementation of a layered winding practically impossible. The model presented in [25] is based on the statistical treatment of simulation results performed by the finite-element analysis (FEA) [26] software and verified by experimental measurements. The common practice in calculating HF copper losses is to calculate two different loss components given by (50) and (51). The resistance factor $Fr_z = R_{{\rm ac},z}/R_{{\rm dc},z}$ of the winding z is calculated by equations presented in [25]

$$P_{{\rm ac},z} = Fr_z R_{{\rm dc},z} I_{z,{\rm rms}}^2 \quad (50)$$

$$P_{{\rm dc},z} = R_{{\rm dc},z} I_{z,{\rm avg}}^2. \quad (51)$$

Therefore, the final power loss ratio is

$$\frac{P_{\rm CPL}}{P_{{\rm PV},w}} = f(n, w, V_{\rm dc}, f_s, B_p, J, r). \quad (52)$$

D. Power Losses Due to the Leakage Inductance of the Transformer

The power loss due to the leakage inductance is given by (53). The energy stored in the leakage inductance is proportional to the energy stored in the main inductance. Therefore, the energy loss ratio is equal to the leakage inductance ratio

$$\frac{P_{L\sigma L}}{P_{{\rm PV},w}} = \frac{L_\sigma}{L_1}. \quad (53)$$

VII. OPTIMIZATION EXAMPLE

By summing the power loss formulas (32), (38), (39), (40), (49), (52), and (53), the total power loss ratio appears. The
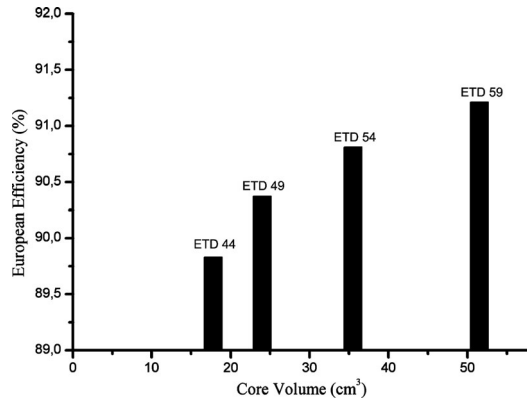
Fig. 5.   European efficiency versus core volume ($V_{\mathrm{dc}} = 25$ V).

TABLE II
INPUT AND OUTPUT SPECIFICATIONS

$P_{PV,nom}$=100W	$V_{dc,min}$=25V	$V_{dc,max}$=40V	V_{acp}=325V

TABLE III
IMPLEMENTED INVERTER PARAMETERS

S_p: IXFH60N20	Core Material: 3f3
S_1,S_2: IXFX26N120	n=0.276
Diode: RHR15120	r=0.15mm
f_s=22.2kHz	str_{pri}=24
N_{pri}=20, (L_1=43μH)	str_{sec}=4
l_g=0.202mm	C_f=150nF
Core Type: ETD44	L_f=10mH

optimization is based on minimizing the total power loss ratio. As it is mentioned earlier, the procedure to optimize the efficiency starts by taking into account the input specifications. By computing the loss formulas, the algorithm calculates the optimum weighted efficiency for all design parameters. In Fig. 5, the exported European efficiencies for different core types can be seen. As the core volume increases, the efficiency gets higher. The core-type ETD 44 is the smallest core that can satisfy the constraint functions. The input and output specifications of the system design can be seen in Table II.

In order to check the validity of the power loss formulas, a laboratory prototype was implemented based on the smallest possible core, thus, the ETD 44

VIII. EXPERIMENTAL RESULTS

The design parameters of the implemented inverter are presented in Table III. The switching sequence of the semiconductors, presented in Fig. 2, is implemented by the DSP microcontroller DSPIC30F4011. In Figs. 6 and 7, the output current measured under nominal power level and minimum input voltage is presented.

In Fig. 6, the current is measured before the output filter, and in Fig. 7 the filter eliminates the HF component of the injected current. In order to verify the loss formulas, a series of precise power measurements were conducted. The instrument that was
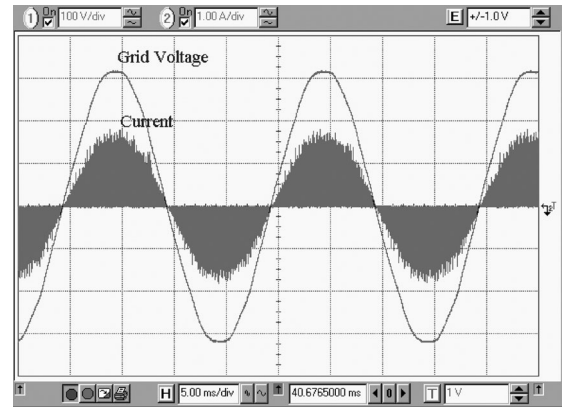

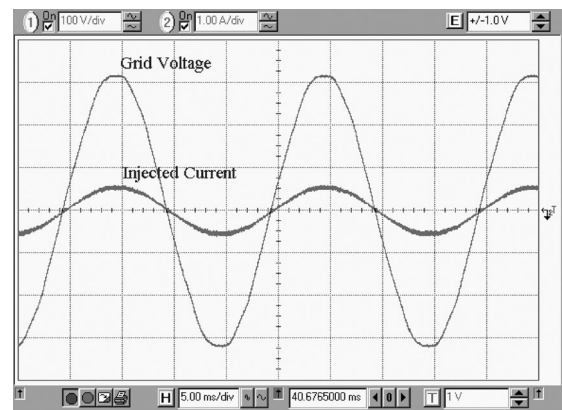Fig. 6.   Output current before the output filter (100 V/div, 1 A/div, 5 ms/div).

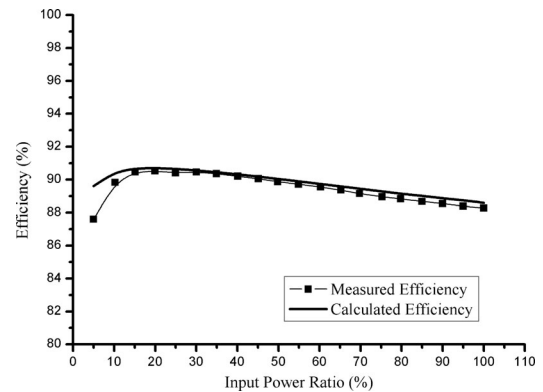Fig. 7.   Output current injected to the utility grid (100 V/div, 1 A/div, 5 ms/div).

Fig. 8.   Calculated and measured efficiency versus power ratio for $V_{\mathrm{dc}} = 25$ V.

used is the precision power analyzer LMG500 of ZES Zimmer manufacturer. The measured and the calculated efficiency values for three different voltage levels can be seen in Figs. 8–10.

As it can be observed, the measured and calculated values converge verifying the loss formulas. The efficiency for every input power level is improving when the input voltage takes higher values. This fact has as a result higher European efficiency when the input voltage is 40 V. The measured and calculated European efficiencies can be seen in Table IV.
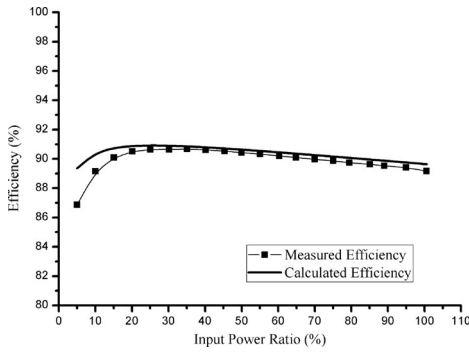
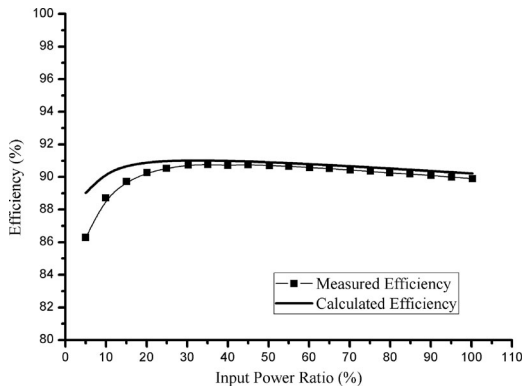Fig. 9. Calculated and measured efficiency versus power ratio for $V_{dc} = 32.5$ V.

Fig. 10. Calculated and measured efficiency versus power ratio for $V_{dc} = 40$ V.

TABLE IV
MEASURED AND CALCULATED EUROPEAN EFFICIENCIES

Input Voltage	Measured Weighted-Efficiency (%)	Calculated Weighted-Efficiency (%)
V_{dc}=25V	89.52	89.83
V_{dc}=32.5V	89.92	90.38
V_{dc}=40V	90.12	90.62
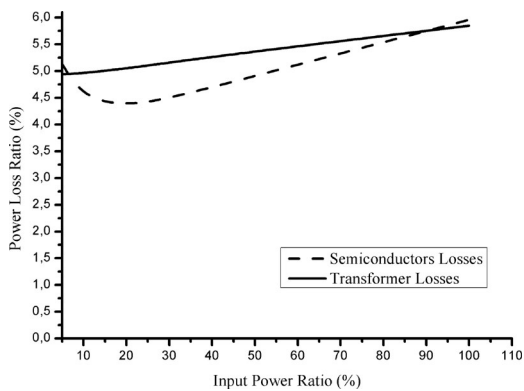
Fig. 11. Power losses of the two main components ($V_{dc} = 25$ V).

In Fig. 11, the discrimination of the calculated power loss between the two main components of the inverter can be observed. The analysis of these power loss ratios can be seen in Figs. 12 and 13.
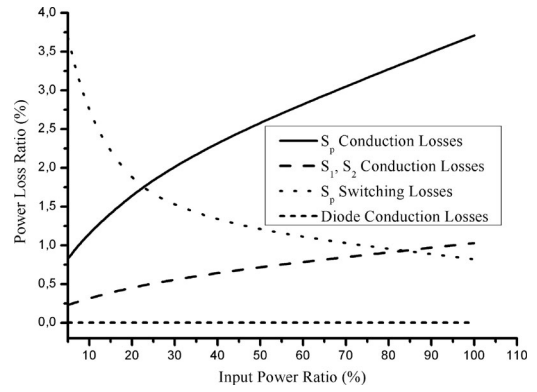

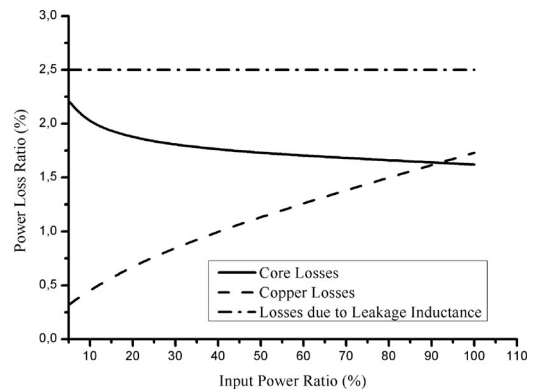Fig. 12. Semiconductors losses analysis ($V_{dc} = 25$ V).

Fig. 13. Transformer losses analysis ($V_{dc} = 25$ V).

IX. CONCLUSION

This paper defines a design methodology for the flyback inverter that clearly specifies the appropriate design parameters to obtain the maximum weighted efficiency. Taking into consideration the input specifications, these consist of the voltage and nominal power of the PV module, the optimization algorithm selects among all the feasible designs that of the maximum weighted efficiency. Feasible design is a set of all the design parameters that satisfy the constraints. The constraints are a set of equations that ensure the proper operation of the flyback under DCM control scheme. The optimal solution corresponds to design parameters from which all other topology variables can be determined. In order to validate the performance of our methodology, an inverter prototype was implemented. As is it already presented, the measured efficiency is very close to the calculated values.

The presented losses equations can be used not only to optimize the efficiency, but also to fulfill extra targets. By using the same equations, many different objective functions can be optimized. For example, for a given input voltage and transformer volume, the maximum feasible nominal power can be determined.

APPENDIX A

We can apply trigonometric function and rewrite the series as follows:

$$\frac{1}{m}\sum_{i=1}^{m}\sin^3\left(\frac{\pi}{m}i\right) = \frac{1}{m}\sum_{i=1}^{m}\left[\frac{3\sin((\pi/m)i) - \sin(3(\pi/m)i)}{4}\right]$$

$$= \frac{3}{4m}\sum_{i=1}^{m}\sin\left(\frac{\pi}{m}i\right) - \frac{1}{4m}\sum_{i=1}^{m}\sin\left(3\frac{\pi}{m}i\right). \quad (A.1)$$

The first term can be rewritten as follows:

$$\frac{3}{4m}\sum_{i=1}^{m}\sin\left(\frac{\pi}{m}i\right)$$

$$= \frac{3}{4m}\frac{\sin((1/2)(m+1)(\pi/m))\sin((1/2)m(\pi/m))}{\sin(\pi/2m)} \quad (A.2)$$

for $m \gg 1$

$$\sin\left(\frac{1}{2}(m+1)\frac{\pi}{m}\right) \approx \sin\frac{\pi}{2} = 1 \quad (A.3)$$

and

$$\sin\frac{\pi}{2m} \approx \frac{\pi}{2m}. \quad (A.4)$$

Therefore, we conclude that

$$\frac{3}{4m}\sum_{i=1}^{m}\sin\left(\frac{\pi}{m}i\right) \approx \frac{3}{4m}\frac{2m}{\pi} = \frac{3}{2\pi}. \quad (A.5)$$

The second term can be rewritten as follows:

$$\frac{1}{4m}\sum_{i=1}^{m}\sin\left(3\frac{\pi}{m}i\right)$$

$$= \frac{1}{4m}\frac{\sin\left((1/2)(m+1)(3\pi/m)\right)\sin\left((1/2)(3\pi/m)m\right)}{\sin(3\pi/2m)} \quad (A.6)$$

for $m \gg 1$

$$\sin\left(\frac{1}{2}(m+1)\frac{3\pi}{m}\right) \approx \sin\frac{3\pi}{2} = -1 \quad (A.7)$$

and

$$\sin\frac{3\pi}{2m} \approx \frac{3\pi}{2m}. \quad (A.8)$$

Therefore, we conclude that

$$\frac{1}{4m}\sum_{i=1}^{m}\sin\left(3\frac{\pi}{m}i\right) = \frac{1}{4m}\frac{2m}{3\pi} = \frac{1}{6\pi}. \quad (A.9)$$

Therefore, the series can be expressed in the simpler form

$$\frac{1}{m}\sum_{i=1}^{m}\sin^3\left(\frac{\pi}{m}i\right) = \frac{4}{3\pi}. \quad (A.10)$$

Moreover, for (23), the series

$$\frac{1}{m}\sum_{i=1}^{m}\sin\left(\frac{\pi}{m}i\right) \approx \frac{3}{2\pi}\frac{4}{3} = \frac{2}{\pi} \quad (A.11)$$

according to the above demonstration.

APPENDIX B

By applying the series trigonometric functions we conclude that

$$\frac{1}{m}\sum_{i=1}^{m}\sin^2\left(\frac{\pi}{m}i\right) = \frac{1}{m}\sum_{i=1}^{m}\left[\frac{1 - \cos\left(2(\pi/m)i\right)}{2}\right]$$

$$= \frac{1}{2} - \frac{1}{4m}\left[\frac{\sin((m+(1/2))(2\pi/m))}{\sin(2\pi/2m)} - 1\right]$$

$$= \frac{1}{2} - \frac{1}{4m}\left[\frac{\sin\left(2\pi + (\pi/m)\right)}{\sin\left(\pi/m\right)} - 1\right] \quad (B.1)$$

for $m \gg 1$.

Therefore, the series can rewritten in the form

$$\frac{1}{m}\sum_{i=1}^{m}\sin^2\left(\frac{\pi}{m}i\right) = \frac{1}{2} - \frac{1}{4m}\left[\frac{\sin\left(\pi/m\right)}{\sin\left(\pi/m\right)} - 1\right] = \frac{1}{2}. \quad (B.2)$$

REFERENCES

[1] J. Gow and C. Manning, "Photovoltaic converter system suitable for use in small scale stand-alone or grid-connected applications," *IEE Proc.-Electr. Power Appl.*, vol. 147, no. 6, pp. 535–543, Nov. 2000.

[2] S. B. Kjaer, J. K. Pedersen, and F. Blaabjerg, "A review of single-phase grid-connected inverters for photovoltaic modules," *IEEE Trans. Ind. Appl.*, vol. 41, no. 5, pp. 1292–1306, Sep./Oct. 2005.

[3] Y. Fang and X. Ma, "A novel PV microinverter with coupled inductors and double-boost topology," *IEEE Trans. Power Electron.*, vol. 25, no. 12, pp. 3139–3147, Dec. 2010.

[4] Z. Liang, R. Guo, J. Li, and A. Q. Huang, "A high-efficiency PV module-integrated DC/DC converter for PV energy harvest in FREEDM systems," *IEEE Trans. Power Electron.*, vol. 26, no. 3, pp. 897–909, Mar. 2011.

[5] R. H. Wills, F. E. Hall, and S. J. Strong, "The AC photovoltaic module," in *Proc. IEEE Photovoltaic Spec. Conf.*, Washington, DC, May 13–17, 1996, pp. 1231–1234.

[6] N. Kasa, T. Iida, and L. Chen, "Flyback inverter controlled by sensorless current MPPT for photovoltaic power system," *IEEE Trans. Ind. Electron.*, vol. 52, no. 4, pp. 1145–1152, Aug. 2005.

[7] A. Ch. Kyritsis, E. C. Tatakis, and N. P. Papanikolaou, "Optimum design of the current-source flyback inverter for decentralized grid-connected photovoltaic systems," *IEEE Trans. Energy Convers.*, vol. 23, no. 1, pp. 281–293, Mar. 2008.

[8] Y.-H. Ji, D.-Y. Jung, J.-H. Kim, C.-Y. Won, and D.-S. Oh., "Dual mode switching strategy of flyback inverter for photovoltaic AC modules," *Proc. Int. Power Electron. Conf.*, pp. 2924–2929, Jun. 21–24, 2010.

[9] *Overall Efficiency of Photovoltaic Inverters,* European Standard EN 50530, 2010.

[10] J. Ejury, *The Selection of MOSFETs for DC-DC Converters,* Neubiberg, Germany: Infineon Technologies, Neubiberg, Germany, Application Note, Feb. 2003.

[11] H. S. Choi, *Design Guidelines for Off-line Flyback Converters Using Fairchild Power Switch (FPS),* San Jose, CA: Fairchild Semiconductor, Application Note AN4137, 2003.

[12] L. H. Dixon, *Magnetics Design for Switching Power Supplies.* Dallas, TX: Unitrode Seminars (TI), 2001.

[13] S. Wolfram, *The mathematica book,* 5th ed. Champaign, IL: Wolfram Media, 2004.

[14] Y. Xiong, S. Sun, H. Jia, P. Shea, and Z. J. Shen, "New physical insights on power MOSFET switching losses," *IEEE Trans. Power Electron.*, vol. 24, no. 2, pp. 525–531, Feb. 2009.

[15] D. A. Grant and J. Gowar, *Power MOSFETS, Theory and Applications.* New York, USA: Wiley-Interscience, 1989, ch. 4.

[16] J. Reinert, A. Brockmeyer, and R. W. A. A. De Doncker, "Calculation of losses in ferro- and ferrimagnetic materials based on the modified Steinmetz equation," *IEEE Trans. Ind. Appl.*, vol. 37, no. 4, pp. 1055–1061, Jul./Aug. 2001.

[17] S. Hui and J. Zhu, "Magnetic hysteresis modeling and simulation using the Preisach theory and TLM technique," in *Proc. IEEE 25th Annu. Power Electron. Spec. Conf.*, Taipei, Taiwan, vol. 2, Jun. 20–25, 1994, pp. 837–842.

[18] D. C. Jiles and D. L. Atherton, "Theory of ferromagnetic hysteresis (invited)," *J. Appl. Phys.*, vol. 55, no. 6, pp. 2115–2120, Mar. 1984.

[19] A. Brockmeyer and L. Schulting, "Modelling of dynamic losses in magnetic material," in *Proc. 5th Eur. Conf. Power Electron. Appl.*, Sep. 13–16, 1993, vol. 3, pp. 112–117.

[20] P. Tenant and J. J. Rousseau, "Dynamic model of magnetic materials applied on soft ferrites," *IEEE Trans. Power Electron.*, vol. 13, no. 2, pp. 372–379, Mar. 1998.

[21] M. Albach, T. Durbaum, and A. Brockmeyer, "Calculating core losses in transformers for arbitrary magnetizing currents a comparison of different approaches," in *Proc. IEEE 27th Annu. Power Electron. Spec. Conf.*, Baveno, Italy, vol. 2, Jun. 23–27, 1996, pp. 1463–1468.

[22] W. A. Roshen, "A practical, accurate and very general core loss model for nonsinusoidal waveforms," *IEEE Trans. Power Electron.*, vol. 22, no. 1, pp. 30–40, Jan. 2007.

[23] J. Li, T. Abdallah, and C. R. Sullivan, "Improved calculation of core loss with nonsinusoidal waveforms," in *Conf. Rec. 36th IEEE Ind. Appl. Conf.*, vol. 4, 30 Sep.–4 Oct. 2001, pp. 2203–2210.

[24] K. Venkatachalam, C. R. Sullivan, T. Abdallah, and H. Tacca, "Accurate prediction of ferrite core loss with nonsinusoidal waveforms using only Steinmetz parameters," in *Proc. IEEE Comput. Power Electron. Conf.*, 2002, pp. 36–41.

[25] G. S. Dimitrakakis, E. C. Tatakis, and E. J. Rikos, "A semiempirical model to determine HF copper losses in magnetic components with nonlayered coils," *IEEE Trans. Power Electron.*, vol. 23, no. 6, pp. 2719–2728, Nov. 2008.

[26] *Opera 2D—User Guide,* Vector Fields Ltd., Kidlington, Oxford, 2003.

Emmanuel C. Tatakis (M'12) received the Dipl. degree in electrical engineering from the University of Patras, Rion-Patras, Greece, in 1981, and the Ph.D. degree in applied sciences from the University of Brussels, Brussels, Belgium, in 1989.

He is currently an Associate Professor in the Department of Electrical and Computer Engineering, University of Patras. His teaching activities include power electronics and electrical machines. His research interests include switch-mode power supplies, resonant converters, HF transformers, power factor correction, electric drive systems and electric vehicles, converters for photovoltaic and wind energy systems, voltage multipliers, educational methods in electrical machines, and power electronics.

Dr. E. C. Tatakis is a member of the European Power Electronics Association (EPE), the Société Royale Belge des Electriciens, and the Technical Chamber of Greece.

Nick P. Papanikolaou (M'09–SM'11) received the Ph.D. degree in electrical engineering from the University of Patras, Rion-Patras, Greece, in 2002.

For a period of four years, he was with the Greek Industry of Electrical Energy. In 2008, he became a Lecturer in the Department of Electrical Engineering, Technological Educational Lamia Institute of Technology, Lamia, Greece, where he is involved in teaching power electronics and electrical drive systems. His research interests include power electronics, renewable energy sources, electrical drive systems, and power quality issues.

Anastasios C. Nanakos received the Dipl. degree in electrical engineering from the University of Patras, Rion-Patras, Greece, in 2005, where he is currently working towards the Ph.D. degree in photovoltaic power generation.

His research interests include photovoltaic power generation, power electronics, high-power-density converters, microinverters, and efficiency optimization techniques.

Mr. Nanakos is a member of the Technical Chamber of Greece.